Available online at www.sciencedirect.com

ScienceDirect

Procedia Structural Integrity 52 (2024) 506–516

Structural Integrity Procedia

www.elsevier.com/locate/procedia

Fracture, Damage and Structural Health Monitoring

Numerical modelling of the cavitation damage in the conrod big end bearing of a high-performance internal combustion engine

Fabio Renso[a], Matteo Giacopini[a], Enrico Bertocchi[a], Daniele Dini[b]

[a]*University of Modena and Reggio Emilia, Engineering Department "Enzo Ferrari", via Vivarelli 10, 41125 Modena (MO), Italy*
[b]*Department of Mechanical Engineering, Imperial College London, Exhibition Road, London, SW7 2AZ, United Kingdom*

Abstract

In this contribution a complementarity formulation for the solution of the elastohydrodynamic problem in the presence of cavitation is employed to investigate the tribological behaviour of the conrod big end bearing in a high-performance internal combustion engine. The continuous effort towards higher engine efficiencies, poses new challenges related to the increased specific loads to which engine components are subjected. In particular, the connecting rod big end bearing is subjected to both high loads and high relative velocity of the mating surfaces. Therefore, its tribological behaviour plays a crucial role. In fact, on one side, possible asperity contact pressures can produce wear of the interested components, and on the other side, a parallel possible cavitation of the lubricant can additionally damage the mating interfaces. Unfortunately for quantifying the cavitation damage, a universally established theory does not exist, even if it is well accepted that it is related to the sudden rapid implosion of the vapour bubbles near the surface. The precise investigation of this damage mechanism is usually neglected in big end bearing analysis since the implosion of the bubbles is difficult to quantify and it is not a standard output of any commercial software. Thus, in this work, a quantitative index previously proposed is reviewed and adopted to quantify the cavitation damage in a connecting rod big end bearing.

Keywords: Type your keywords here, separated by semicolons ;

1. Introduction

Reducing friction is one of the key strategies for increasing engine efficiency and for meeting strict emission regulations, along with turbocharging, downsizing, and hybridization (Barbieri et al. 2019; Bianco et al. 2023; Mangeruga et al. 2023 a). The connecting rod big end bearing is a major source of friction in the crank mechanism due to the high loads and relative velocities involved. Additionally, possible low pressures areas within the fluid film

10.1016/j.prostr.2023.12.050

can cause cavitation. Reynolds equation is commonly used to model lubrication in bearings, since main assumptions such as a small oil film thickness and a low Reynolds number are usually satisfied. Various formulations have been proposed to accurately simulate the phenomenon of cavitation (Elrod 1981; Bayada et al. 2001; Ausas et al. 2007; Giacopini et al. 2010). In cavitated regions, the fluid is usually assumed to be subjected to a constant pressure equal to the cavitation pressure. At the limits of this regions, where the fluid reforms, cavitated bubbles suddenly implode, thus possibly causing erosion of the components. Unfortunately, there is not a universal theory for predicting and quantifying the corresponding damage induced by the bubbles collapse.

In this research, a numerical procedure to model the cavitation damage in the conrod big end bearing of a high-performance internal combustion engine is investigated. First, a review of the available literature is presented, and the specific cavitation damage index adopted is described. As a next step, the numerical model developed employing a dedicated procedure is given. Parallelly, the setup of a complete and detailed Multibody model of the crank mechanism using the commercial software AVL Excite Power Unit is presented, and results of this model are used to validate the ones obtained with the proposed numerical code. Specifically, a dedicated section focuses on the results obtained and their post-processing. The corresponding cavitation damage plots are compared and commented. Finally, some conclusions end the paper.

Nomenclature

CDI	Cavitation Damage Index
Cr_d	Crush relief depth
Cr_w	Crush relief width
EHL	Elastohydrodynamic Lubrication
V_{vap}	Volume of the cavitation bubbles
h_t	Nominal thickness
h_l	Lemon shape thickness
α_l	Lemon shape angle
θ	Shell angle

1.1. Literature Review

In the past, various studies proposed an estimation of the cavitation damage with different fields of application. In particular, Tao and Appledoorn, (Tao et al. 1971) concluded that the impact with liquid jets triggers a fatigue process that causes cavitation damage. The bubbles collapse in areas of high pressure, due to the pressure difference between the inside of the bubble and the outside, and a microjet arises. Factors such as surface tension and vapor pressure are therefore relevant for the investigation of this phenomenon. The surface energy of the bubble is another index of the damage that its collapse can cause, together with liquid density and bulk-modulus. It has been demonstrated (Zhuang et al. 2023) that cavitation erosion is characterized by an incubation period during which no damage has yet occurred, followed by a phase with a constant wear rate. The incubation is linked to the fatigue resistance of the material, while the approximately constant wear rate which occurs when the phenomenon is triggered is linked to the hardness of the material and the value of the tensile strength. The schematic process of the bubble collapse is given in (Dular et al. 2019) and it is depicted in Fig. 1.

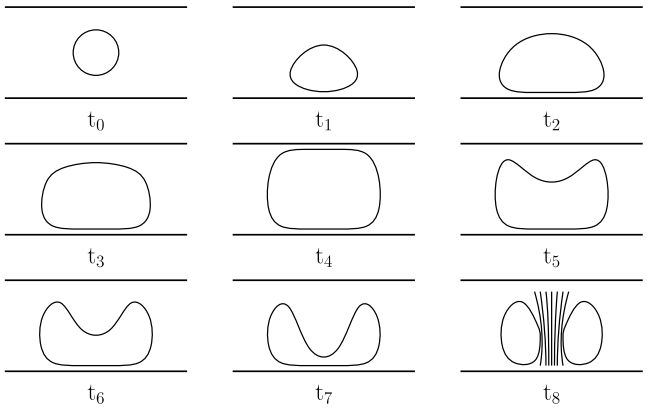

Fig. 1. Mechanism of microjet formation at bubble collapse, as in (Dular et al. 2019)

Models such as those proposed by Dular, Stoffel, Sirok (Dular et al. 2006, 2019), Pereira, Avellan, Doupont (Pereira et al. 1998), try to predict the erosion damage, based on the energy transfer model. The fundamental idea behind these models is that energy is absorbed by the plastic deformation of the material surface. When the impact pressure is higher than the yield strength of the material, a plastic wave propagates, which causes the appearance of small craters called cavities. Recently, attention has been drawn to the possible interaction of groups of bubbles. If the frequency of cavitation events increases, the bubbles can interact with each other, forming cavitation clouds (Patella et al. 2012). Clouds, due to perturbations that propagate in the flow, periodically form and collapse, causing destructive effects, with relative greater noise and surface damage. Based on the energetic approaches presented in (Pereira et al. 1998; Dular et al. 2006; Patella et al. 2012), a Cavitation Damage Index (CDI) has been proposed by some of the authors in a previous research (Dini et al. 2014) and defined as:

$$CDI = \sum_{t=0}^{t_{end}} \left| \frac{dV_{vap}}{dt} \right| \leftrightarrow V_{vap}\big|_t > 0 \ \wedge \ V_{vap}\big|_{t+dt} = 0 \tag{1}$$

In particular, V_{vap} represent the volume occupied by the cavitation bubbles. Actually, the proposed index represents the summation of the variation of the volume of the bubbles across each event of fluid reformation (bubbles collapse) along a single engine cycle. This formulation is directly linked to those presented in past research with the only difference that the variation of pressure in the cavitated region is assumed to be zero and thus some terms can be neglected, see (Patella et al. 2012) for further details. This formulation accumulates the damage induced along the whole engine cycle. In particular, this procedure is not so far from those applied in classical fatigue approaches to take into account the superposition of multiple fatigue cycle within a single engine cycle (Miner 1945; Brown et al. 1973; Downing et al. 1982; Giacopini et al. 2015).

2. Methodology

This contribution aims at providing a methodology to assess the cavitation damage in the connecting rod big end bearing of a high-performance internal combustion engine. In particular, two connecting rods are studied for the same engine, having different materials and (slightly) different shapes: one in titanium and one in steel. Consequently, also the design of the crankshaft is different between the two engine configurations since the counterweight shape and size will be different. Fig. 2 (a) depicts the steel connecting rod, while Fig. 2 (b) shows the corresponding crankshaft.

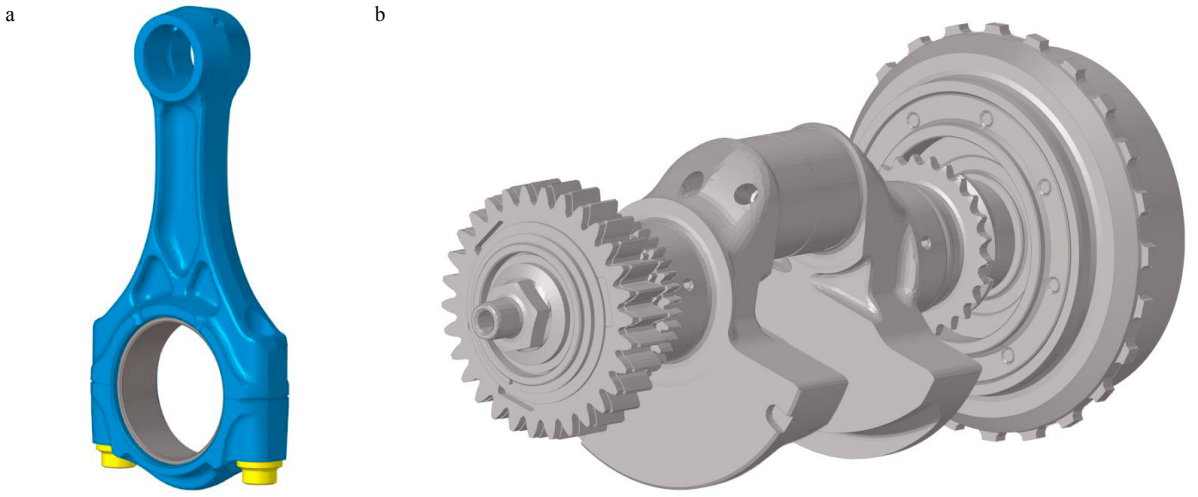

Fig. 2. (a) steel conrod; (b) crankshaft adopted with the steel conrod.

As a first step, the connecting rods mounting procedure has been replicated to obtain exactly the bearing shape once mounted on the crankshaft. A Finite Element model has been therefore prepared for this purpose. Subsequently, the connecting rods and the crankshafts stiffness have been statically condensed to their interface degrees of freedom, i.e. the inner nodes of the bearing and the outer nodes of the crank pin. The compliance of the connecting rod and the crankshaft have been then combined to obtain a compliance matrix that considers the deformation of both the components. Finally, this complete compliance matrix, has been introduced in a dedicated code which solves a mass-conserving formulation of the Reynolds equation in the presence of cavitation, together with the asperity contact problem, considering the actual gap between the two surfaces, the instantaneous sliding velocity and the load applied to the coupling. Conversely from previous works (Bertocchi et al. 2012; Profito et al. 2019), the inertial effects associated with the rigid body motions are not implicitly accounted for in the external loads. Thus, the external load in this dissertation is just related to the gas pressure acting on the piston and on the unmodelled inertias (piston pin, piston and rings). The effects related to the presence of a distributed inertia are considered as forces acting on the condensed nodes whose amplitude and direction depend on the engine speed and on the crank angle position, as in (Bonneau et al. 1995).

Parallelly, a second model has been developed adopting the commercial software AVL Excite. In this case a Craig-Brampton dynamic condensation has been adopted to consider deformability and inertia of the involved components while the Reynolds equation governing the lubricating behaviour of the hydrodynamic bearing is solved with the standard p-θ algorithm (Elrod 1981) and the asperity contact problem is accounted for considering the standard Greenwood-Tripp approach (Greenwood et al. 1970).

2.1. Tightening Procedure

To guarantee a correct behaviour of the conrod big end bearing, a suitable tightening procedure has to be defined for both conrod big end inner surface machining and for the bearing installation when the conrod is assembled with the crankshaft. Specifically, starting from a semifinished component, the connecting rod bolts are tightened, thus deforming the big end shape. Then, the small end is fixed at a reference position, and a mill is used to machine the big end to a cylindrical shape. This cylinder has its centre at a distance from the small end equal to the connecting rod nominal length and its diameter is equal to the nominal diameter of the big end. This procedure ensures that the connecting rod big end has a cylindrical shape when the bolts are tightened. At this point the connecting rods are usually packed and prepared for shipping. When the conrod is then assembled with the crankpin, the bolts are removed, the two half bearings are mounted in their respective positions, and the bolts are tightened again. Considering that the two half bearings have a certain circumferential over-extent (crush height) for guaranteeing their correct press fitting,

they will partially absorb the bolt tightening force thus slightly modifying the perfectly cylindrical shape of the big end.

To exactly grasp the shape of the gap between the connecting rod big end bearing and the crank pin, this outlined procedure has been reproduced via a Finite Element simulation. In particular, a first tightening has been performed, following which the nodes belonging to the big end inner surface have been projected to a cylindrical surface having the nominal diameter and placed at the nominal connecting rod length with respect to the small end centre position. This procedure mimics the machining process of the big end, and the coordinates of the nodes have been stored in a text file. Subsequently, restarting from the original Finite Element model, the tightening has been repeated. At this point, the nodal coordinates have been retrieved from the previous simulation and the big end nodes have been moved, stress free, to the perfectly cylindrical stored positions. As a next step, the bearing has been press fitted into the connecting rod big end.

Additionally, the specific lemon-shaped profile is then superimposed onto the deformed diameter of the bearing obtained through the above-described procedure. In fact, the bearing has a non-uniform thickness, as shown in Fig. 3, which depicts a half bearing with reference dimensions used for profile definition. The thickness of the bearing decreases from its vertical section, h_t, towards the horizontal split, passing through a controlled section of thickness $h_t - h_l$, thus producing a parallel increase of the gap between the mating surfaces of the connecting rod bearing and the crank pin. A further local reduction of the bearing thickness is also introduced in the region of the horizontal split having determined width, Cr_w, and depth, Cr_d, with the aim of absorbing possible local bearing deformations promoted by the mounting procedure.

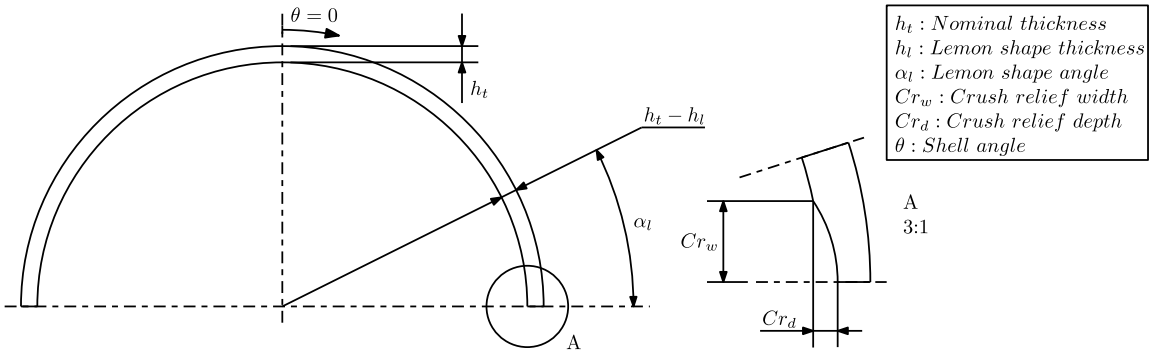

Fig. 3. Schematics of a half bearing profile.

Finally, a further simulation step has been introduced in which a distributed temperature of 120°C has been applied to the involved components to take into account the thermal expansion induced by the operating condition. This last step could be neglected when the components involved exhibit the same thermal expansion coefficients, i.e. both conrod and crankshaft made of steel, but it can play a crucial role in the gap shape definition when conrod and crankshaft are made of different materials, i.e. titanium conrod and steel crankshaft (Bianco et al. 2022).

In this sense, Fig. 4 depicts a comparison of the gap profile in cold and hot conditions for both titanium and steel connecting rods. Due to the different thermal expansion, the titanium connecting rod bearing loses some of the radial clearance since the crankshaft is produced in steel which has a 20% higher thermal expansion coefficient if compared to the one of titanium. Figure 4 (a) shows the clearance profile of the titanium connecting rod bearing in cold (as assembled) condition, while Fig. 4 (b), refers to the corresponding hot condition. A variation can be appreciated especially if we look at the areas of crush relief, i.e. at 90° and at 270° shell angle. On the other hand, when the steel connecting rod is addressed, no significant variations can be appreciated between the cold, Fig. 4 (c), and the hot, Fig. 4 (d), condition.

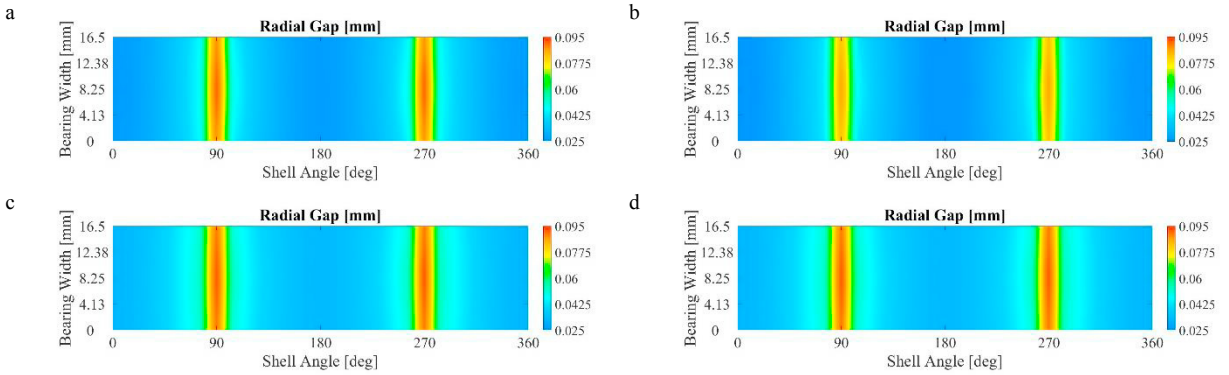

Fig. 4. Radial gap between the titanium connecting rod big end bearing and the crankpin in cold condition (a) and in operating condition (b); radial gap between the steel connecting rod big end bearing and the crankpin in cold condition (c) and in operating condition (d);

2.2. Governing Equations and Numerical Procedure

The developed procedure considers at each crank angle a different stiffness matrix and different problem parameters for the system under investigation. In particular, at each crank angle, a corresponding sliding velocity, gas pressure, acceleration, inertial load distribution and supply hole position are employed. All this information has been retrieved from a quasi-static analysis performed in advance. At this point the mixed lubrication problem has been evaluated. Starting from the fluid domain, the mass-conserving formulation developed by Giacopini et al. (Giacopini et al. 2010; Bertocchi et al. 2013) has been implemented adopting bilinear quadrilateral elements and transformed into a system of nonlinear equations through a Fischer-Burmeister complementarity function (Fischer 1995). Simultaneously, the load balance on the component, considering the hydrodynamic pressure, the load from the piston, the inertial loads and the resulting asperity contact pressure has been evaluated. The asperity contact is again managed by a Fischer-Burmeister function that considers the complementarity between the asperity pressure and the gap. Given the fact that minor differences could be encountered when adopting a simplified linear complementarity approach for the asperity contact instead of the commonly employed more complex Greenwood/Tripp asperity contact model (Ferretti et al. 2019; Ubero‐Martínez et al. 2022), and considering that this dissertation focuses on the cavitation damage, the former has been adopted and implemented in the presented procedure. The Jacobian matrix of the problem has been evaluated and used to predict the values of the variables for the next iteration adopting a Newton method; in fact, the benefits of its quadratic convergence overcome the cost of the evaluation of the Jacobian (Press et al. 2007). The gap, the hydrodynamic pressure and the void fraction are used as variables and the residuals are evaluated for each unconstrained node in terms of load balancing, fluid mass conservation and complementarity conditions. The outlined system of nonlinear equations has been solved simultaneously for all the quantities involved. Thus, every Newton iteration returns a new value for each quantity, namely: pressure, void fraction, gap shape, asperity contact pressure. The outlined method also differs from those usually adopted for the solution of elastohydrodynamic lubrication problems where partitioned solvers are usually encountered (Ferretti et al. 2018; Profito et al. 2019). For the sake of robustness, however, a backstepping method has been introduced to avoid possible oscillations of the results.

The outputs of the solver are the radial gap distribution, the asperity contact pressure, the hydrodynamic pressure and the void fraction. In standard EHL analysis, results in terms of the average values of these quantities are usually commented (Mastrandrea et al. 2015). In this case, a dedicated post processing has been performed for the void fraction in order to compute the Cavitation Damage Index previously introduced and similarly to (Dini et al. 2014).

2.3. AVL Excite Multibody Model

In the automotive world, the use of multibody simulations is widespread. These programs reduce the time to market by speeding up the development of all the components involved. In particular, a Multibody dynamic model is hereby presented of the whole crank mechanism. This model has been realized through the commercial software AVL Excite Power Unit. The aim of the simulation is the Elastohydrodynamic analysis of the connecting rod big end bearing. Stiffness and inertia of the various components involved have been included by performing a Craig-Brampton dynamic condensation in the Finite Element realm. The inputs of the model are the combustion pressure applied on the piston and the initial revving speed of the crankshaft. The outputs obtained with this model are then compared with the ones resulting from the above presented ad-hoc developed procedure.

3. Comparison

As a first step, the time averaged results obtained with the different instruments outlined before, namely the ad-hoc developed code and AVL Excite Power Unit, are considered. Specific simulations have been performed for both the titanium and steel connecting rod, while spanning all the operating revving regimes of the engine under investigation. For the sake of conciseness, however, just the results related to the highest revving speed, i.e. 12500 rpm, are presented.

3.1. Steel Connecting Rod

Starting from the steel connecting rod, Fig. 5 depicts the average hydrodynamic, asperity and total pressure obtained with the two outlined methodologies at 12500 rpm. The results related to AVL Excite Power Unit, shown in Fig. 5 (a) almost perfect match with those obtained with the developed procedure, see Fig. 5 (b). These preliminary results highlight the robustness of the developed procedure, that is able to grasp all the major effects involved in the tribological behaviour of the steel connecting rod bearing.

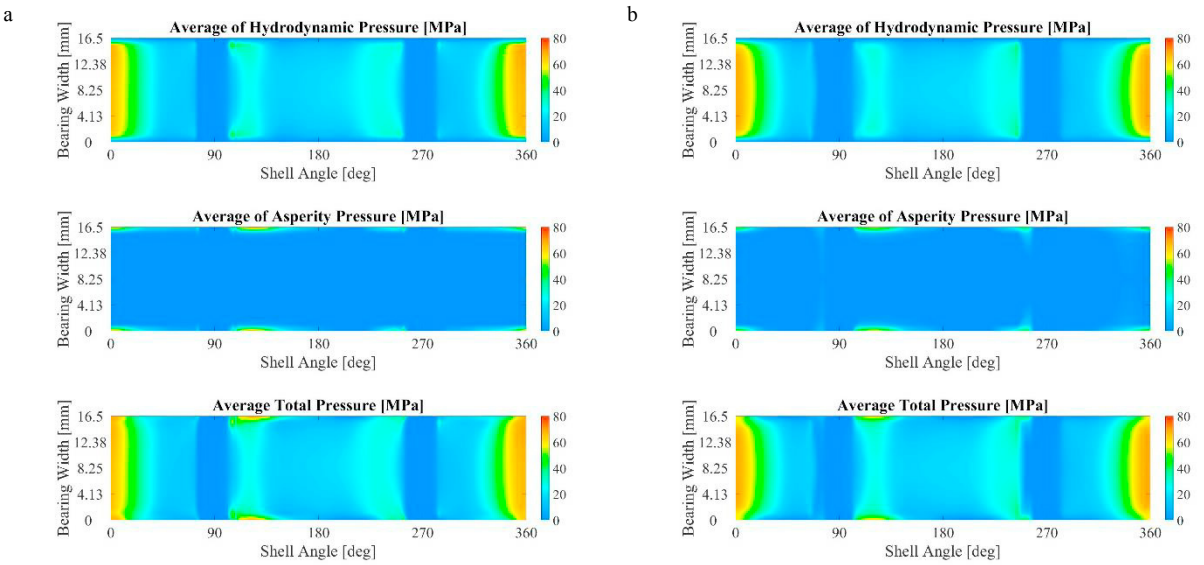

Fig. 5. Cycle average hydrodynamic, asperity and total pressure for the steel connecting rod, obtained through AVL Excite (a) and with the presented procedure (b)

3.2. Titanium Connecting Rod

The titanium connecting rod is then addressed. This connecting rod has almost the same geometry of the one produced in steel. The major difference between the two connecting rods is the material. With respect to steel, titanium exhibits about half the stiffness and half the density. So that, even with a very similar Young modulus over density ratio, the compliance of the connecting rod will be greater, when titanium is adopted. In fact, when the same load is applied it will deform more than the steel component addressed in the section above. The results related to the titanium connecting rod are depicted in Fig. 6. In particular, Fig. 6 (a) shows the results obtained through AVL Excite while Fig. 6 (b) displays those obtained through the developed procedure. The effect of the increased compliance of the titanium connecting rod can be appreciated when results of Fig. 6 are compared to those of Fig. 5. In fact, a wider and smoother high-pressure region is registered in the titanium connecting rod close to the uppermost part of the bearing i.e. 0°/360° shell angle which can be explained if we consider the higher deformability of the titanium connecting rod big end that easily wraps the crankpin under the effect of the distributed inertial load. Moreover, also with this component, the results of the two methods adopted almost perfectly match each other.

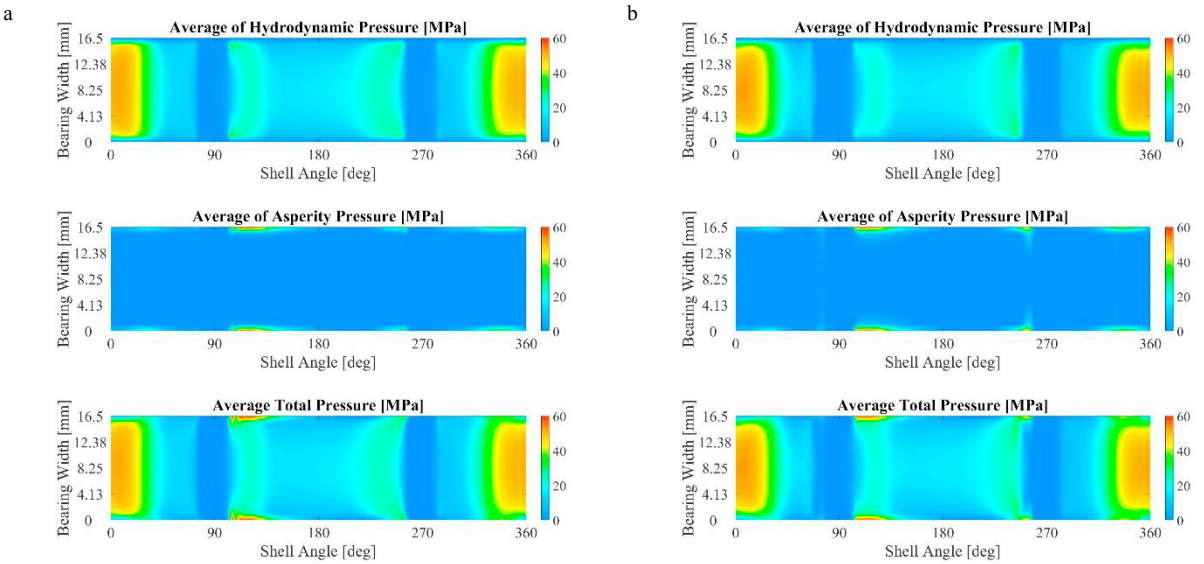

Fig. 6. Cycle average hydrodynamic, asperity and total pressure for the titanium connecting rod, obtained through AVL Excite (a) and with the presented procedure (b)

4. Cavitation Damage

Given the assessed reliability of the developed procedure, as a last step, a Cavitation Damage Index has been computed. Following the definition of the damage on the component due to cavitation, Eq. 1, a dedicated post processing has been performed of the results. Figure 7 depicts the CDI for the steel connecting rod at various revving speeds. In particular, Fig. 7(a) depicts the Cavitation Damage Index at 8500 rpm, Fig. 7(b) at 10500 rpm, Fig. 7(c) at 11500 rpm and Fig. 7(d) at 12500 rpm. Please note that all the results have been normalised with respect to the maximum value computed. From this first comparison, it is clear that the damage increases as the revving speed increases. In fact, cavitation arises predominantly when the velocity of the fluid is high. The regions where the Cavitation Damage Index exhibits the maximum value are those of the crush relief region. In that position, a reforming of the oil film occurs frequently during a single engine cycle and thus, the CDI exhibits a high value. Moreover, since the gap is higher in that region, also the volume occupied by the bubbles is higher and thus reformation becomes more abruptly. This fact is also aligned with experimental results presented in (Dini et al. 2014).

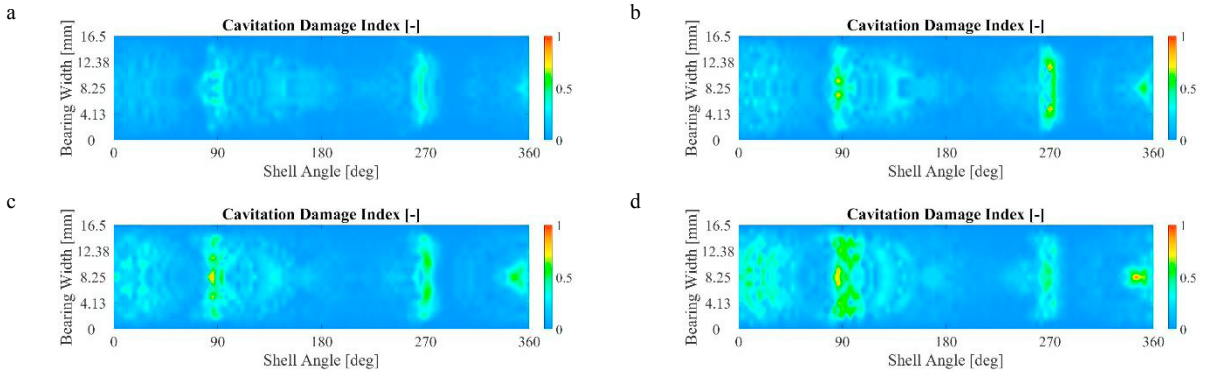

Fig. 7. Cavitation Damage Index contour plot obtained with the presented procedure for the steel connecting rod at 8500 rpm (a), 10500 rpm (b), 11500 rpm (c) and 12500 rpm (d).

Figure 8 (a) shows the cavitation damage index for the titanium connecting rod at 12500 rpm and, the same scenario obtained through AVL Excite is depicted in Fig. 8 (b). Even if the value of the asperity and hydrodynamic pressures are very similar between AVL Excite and the presented procedure, the corresponding CDI plot present some differences even if the main regions where the cavitation damage index is high are correctly grasped by both methods. In particular, on the left the presented procedure estimates a wider region with a high Cavitation Damage Index. On the other hand, the results obtained through AVL Excite, present a higher local maximum. On the crush relief region, at 90°, the presented procedure returns again a higher CDI while, at 270° the resulting value is lower, when compared with the results of Fig. 8 (b). These small discrepancies of the results may be ascribed to several factors. First of all, the formulation adopted for the solution of the hydrodynamic problem is different: AVL Excite exploits the p-θ formulation (Elrod 1981), while the presented procedure adopts a linear complementarity approach (Giacopini et al. 2010). Moreover, the computational grid is different for the fluid domain in the two procedures: AVL Excite adopts a finite difference based multigrid solver able to exploit a fluid mesh finer than the solid mesh, while the developed procedure, adopts a finite element based fixed grid for both the solid and the fluid domain. Additionally, the multibody solver is able to grasp not only the acceleration related to the rigid body motion of the connecting rod but also the instantaneous accelerations related to the relative motion of the bearing and the crankpin, similarly to (Profito et al. 2019). Finally, the shaft misalignment, the instantaneous variation of the crankshaft velocity and the presence of any system resonances can only be obtained with a multibody model (Mangeruga et al. 2023 b).

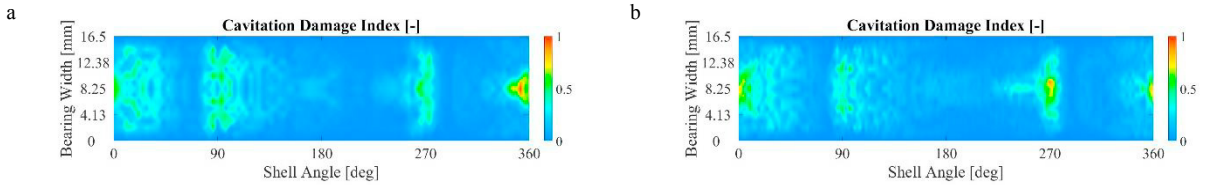

Fig. 8. Cavitation Damage Index contour plot obtained with the presented procedure for the titanium connecting rod at 12500 rpm (a) and for the same configuration through AVL Excite (b).

Considering that the results corresponding to the two materials presented above are not perfectly comparable each other, due to the effect of the different tightening procedure and the different thermal expansion on the definition of the clearance under operating conditions, an additional set of simulations has been performed under identical conditions. For these simulations, the same clearance profile has been artificially imposed to univocally define the effect of the adoption of a different material for the connecting rod manufacturing. In fact, the gas pressure and inertial loads due to the unmodelled masses were consistent for all models, and the only differences can be attributed to the load due to the distributed inertia of the connecting rod together with the stiffness of the component, both of which are lower for the titanium connecting rod. Figure 9 shows the results of these simulations for the two connecting rods.

Specifically, Fig. 9 (a) depicts the steel connecting rod while Fig. 9 (b) shows the titanium connecting rod. Results appear to be both qualitatively and quantitively similar, even if slightly higher values are registered for the titanium connecting rod.

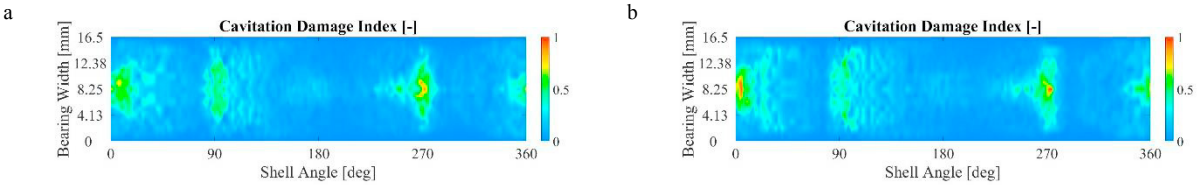

Fig. 9. Cavitation Damage Index contour plot at 12500 rpm for the steel connecting rod (a) and for the titanium connecting rod (b).

4. Conclusion

The cavitation damage evaluation has been performed on a big end bearing belonging to a high-performance internal combustion engine. This activity was demanded to assess the possibility of quantifying this uncommon damage on bearing. The problem has been addressed through two different approaches for two different systems at four different revving speed. With both the procedures adopted for the solution of the elastohydrodynamic problem, namely the developed procedure and the commercial software AVL Excite, the obtained results are very close to each other. Through a dedicated post-processing, the proposed Cavitation Damage Index has been computed. The results were compared with each other to ensure the robustness of the models and to find the influence of the connecting rod material and the operating regime on the cavitation damage. In particular, the crucial factor seems to be the engine speed: at higher velocities, the cavitation damage is greater for both the steel and the titanium connecting rods. To make the results fully comparable in terms of connecting rod material, further tests were performed artificially assuming the same clearance profile in operating conditions for both the connecting rods. The results obtained reveal that the titanium connecting rod has a (slightly) higher risk of incurring this damage mechanism. Finally, when the results obtained with the developed procedure are compared with those from AVL Excite, the same critical regions are highlighted by both the procedures, albeit with slightly different values of the Cavitation Damage Index. In conclusion, the current study sheds light on the fundamental mechanisms of cavitation erosion and provides a framework for predicting the damage caused by cavitation. However, there are still areas that need to be explored further. Future research could include the adoption of the Greenwood-Tripp asperity contact model even in the ad-hoc developed procedure together with the inclusion of thermal effects, giving rise to a thermo-elastohydrodynamic model. This would allow for a more accurate prediction of the tribological behaviour of bearings in general, leading to better design strategies and improved reliability of engineering systems.

Acknowledgements

The authors acknowledge AVL List GmbH for the software AVL EXCITE provided for the calculation of the Multibody simulations.

References

Ausas, R., Ragot, P., Leiva, J., Jai, M., Bayada, G., Buscaglia, G. C., 2007. The Impact of the Cavitation Model in the Analysis of Microtextured Lubricated Journal Bearings. Journal of Tribology 129, 868–875.

Barbieri, S. G., Giacopini, M., Mangeruga, V., Bianco, L., Mastrandrea, L. N., 2019. A Simplified Methodology for the Analysis of the Cylinder Liner Bore Distortion: Finite Element Analyses and Experimental Validations. SAE Technical Papers , Vol. 2019-Septe.

Bayada, G., Chambat, M., 2001. A finite element algorithm for cavitation in hydrodynamic lubrication. Revue Europeenne des Elements 10, 653–678.

Bertocchi, L., Giacopini, M., Dini, D., 2012. Analysis of the Lubrication Regimes at the Small End and Big End of a Connecting Rod of a High Performance Motorbike Engine. ASME/STLE 2012 International Joint Tribology Conference . American Society of Mechanical Engineers, pp. 229–231.

Bertocchi, L., Dini, D., Giacopini, M., Fowell, M. T., Baldini, A., 2013. Fluid film lubrication in the presence of cavitation: A mass-conserving two-dimensional formulation for compressible, piezoviscous and non-Newtonian fluids. Tribology International 67, 61–71.

Bianco, L., Barbieri, S. G., Mangeruga, V., Giacopini, M., Capoccia, G., 2022. Influence of the thermal deformation on the lubricating performance of the piston-gudgeon pin interface in an internal combustion engine. Tribology International 174, 107719.

Bianco, L., Barbieri, S. G., Mangeruga, V., Perez, F. F., 2023. Influence of the Pressure Gradient During Combustion on the Fatigue Behaviour of an Internal Combustion Engine Piston. AIP Conference Proceedings

Bonneau, D., Guines, D., Freˆne, J., Toplosky, J., 1995. EHD Analysis, Including Structural Inertia Effects and a Mass-Conserving Cavitation Model. Journal of Tribology 117, 540–547.

Brown, M. W., Miller, K. J., 1973. A Theory for Fatigue Failure under Multiaxial Stress-Strain Conditions. Proceedings of the Institution of Mechanical Engineers 187, 745–755.

Dini, D., Mastrandrea, L. N., Giacopini, M., Bertocchi, E., 2014. Numerical investigation of the cavitation damage in a high performance engine conrod big end bearing via a mass-conserving complementarity algorithm. Society of Tribologists and Lubrication Engineers Annual Meeting and Exhibition 2014 2, 586–589.

Downing, S. D., Socie, D. F., 1982. Simple rainflow counting algorithms 31–40.

Dular, M., Stoffel, B., Širok, B., 2006. Development of a cavitation erosion model. Wear 261, 642–655.

Dular, M., Požar, T., Zevnik, J., Petkovšek, R., 2019. High speed observation of damage created by a collapse of a single cavitation bubble. Wear 418–419, 13–23.

Elrod, H. G., 1981. A Cavitation Algorithm. Journal of Lubrication Technology 103, 350–354.

Ferretti, A., Giacopini, M., Mastrandrea, L., Dini, D., 2018. Investigation of the Influence of Different Asperity Contact Models on the Elastohydrodynamic Analysis of a Conrod Small-End/Piston Pin Coupling. SAE International Journal of Engines 11, 2018-01–0836.

Ferretti, A., Giacopini, M., Dini, D., Fantoni, S., 2019. Experimental Measurement of Roughness Data and Evaluation of Greenwood/Tripp Parameters for the Elastohydrodynamic Analysis of a Conrod Small-End/Piston Pin Coupling. SAE Technical Paper Series , Vol. 1pp. 586–597.

Fischer, A., 1995. A Newton-type method for positive-semidefinite linear complementarity problems. Journal of Optimization Theory and Applications 86, 585–608.

Giacopini, M., Fowell, M. T., Dini, D., Strozzi, A., 2010. A Mass-Conserving Complementarity Formulation to Study Lubricant Films in the Presence of Cavitation. Journal of Tribology 132.

Giacopini, M., Sissa, S., Rosi, R., Fantoni, S., 2015. Influence of different temperature distributions on the fatigue life of a motorcycle piston. Proceedings of the Institution of Mechanical Engineers, Part D: Journal of Automobile Engineering 229, 1276–1288.

Greenwood, J. A., Tripp, J. H., 1970. The Contact of Two Nominally Flat Rough Surfaces. Proceedings of the Institution of Mechanical Engineers 185, 625–633.

Mangeruga, V., Renso, F., Raimondi, F., Giulio, S., Giacopini, M., 2023a. Influence of the Crankshaft Dynamic Phenomena on the Fatigue Behaviour of a Transmission Chain in a Hybrid Power Unit. AIP Conference Proceedings

Mangeruga, V., Renso, F., Barbieri, S. G., Giacopini, M., Raimondi, F., 2023b. Numerical Investigation of the Dynamic Effects on the Fatigue Behaviour of a Transmission Chain in a Hybrid Power Unit. Journal of Multiscale Modelling

Mastrandrea, L. N., Giacopini, M., Dini, D., Bertocchi, E., 2015. Elastohydrodynamic Analysis of the Conrod Small-End of a High Performance Motorbike Engine via a Mass Conserving Cavitation Algorithm. Volume 15: Advances in Multidisciplinary Engineering . American Society of Mechanical Engineers, pp. 1–11.

Miner, M. A., 1945. Cumulative Damage in Fatigue. Journal of Applied Mechanics 12, A159–A164.

Patella, R. F., Archer, A., Flageul, C., 2012. Numerical and experimental investigations on cavitation erosion. IOP Conference Series: Earth and Environmental Science 15.

Pereira, F., Avellan, F., Dupont, Ph., 1998. Prediction of Cavitation Erosion: An Energy Approach. Journal of Fluids Engineering 120, 719–727.

Press, W. H., Teukolsky, S. A., Vetterling, W. T., Flannery, B. P., 2007. *Numerical Recipes 3rd Edition: The Art of Scientific Computing*. Cambridge University Press , Vol. 1.

Profito, F. J., Zachariadis, D. C., Dini, D., 2019. Partitioned fluid-structure interaction techniques applied to the mixed-elastohydrodynamic solution of dynamically loaded connecting-rod big-end bearings. Tribology International 140, 105767.

Tao, F. F., Appledoorn, J. K., 1971. Cavitation Erosion in a Thin Film as Affected by the Liquid Properties. Journal of Lubrication Technology 93, 470–477.

Ubero-Martínez, I., Rodríguez-Tembleque, L., Cifuentes-Rodríguez, J., Vallepuga-Espinosa, J., 2022. 3D thermoelastic solids under non-linear interface thermal and orthotropic frictional contact conditions. International Journal for Numerical Methods in Engineering 123, 2631–2659.

Zhuang, D. dong, Zhang, S. hao, Liu, H. xia, Chen, J., 2023. Cavitation erosion behavior and anti-cavitation erosion mechanism of NiTi alloys impacted by water jet. Wear 518–519, 204631.